Supporting Information

"All-in-One" Polypyrrole Pillar Hybridization Flexible Membranes on Multimodal Tactile Sensor for Wearable Energy Storage Devices and Human Machine Interfaces

Jing Wei[1,2,3#], Youchao Teng[1#], Lian Han[3], Jiawei Ge[1,4], Zhilei Zhang[1], Yongzan Zhou[1], Changyan Xu[2*], Dagang Li[2*], Kam C Tam[3*], Yimin A. Wu[1*]

[1] Department of Mechanical and Mechatronics Engineering, Waterloo Institute for Nanotechnology, Materials Interfaces Foundry, University of Waterloo, Waterloo, Ontario, N2L 3G1, Canada

[2]College of Material Science and Engineering, Nanjing Forestry University, 159 Longpan Road, Nanjing, Jiangsu 210037, China

[3] Department of Chemical Engineering, University of Waterloo, Waterloo, Ontario, N2L 3G1, Canada

[4] College of Materials Science and Technology, Jiangsu Key Laboratory of Materials and Technology for Energy Conversion, Nanjing University of Aeronautics and Astronautics, 29 Jiangjun Ave, Nanjing, 211106, China

Table of contents

1. Experimental

1.1. Materials

Bamboo powders derived from moso bamboo were obtained from Zhejiang (Lishui, China) and sifted in a 60-mesh sieve. Graphene oxide (GO) dispersion was purchased from Hangzhou Gaoxi Technology Co., Ltd. Pyrrole monomers (Py). Hydroiodic acid (HI, 58%) was purchased from Shanghai Aladdin Biochemical Technology Co., Ltd. P-toluene sulfonate acid (p-TSA, $C_7H_8O_3S$) was obtained from Shanghai McLean Biochemical Technology Co., Ltd. Polyvinyl alcohol (PVA, average Mw 89 000−98 000) was acquired from Sigma-Aldrich Co., Ltd. Sulfuric acid (H_2SO_4), acrylic acid (AA) and Potassium persulfate ($K_2S_2O_8$) were purchased from Nanjing Chemical Reagent Co., Ltd. All the reagents were used directly without further purification.

1.2 Preparation of RGO/CNFs composite membranes

The preparation method of CNFs was obtained from our previous study. The mixture of GO and CNFs was stirred with a different weight ratio of 1:0, 1: 0.25, 1: 0.5, 1: 0.75 and 1:1, respectively, and then the GO/CNFs suspension (1 mg mL^{-1}) was operated for 40 min by ultrasonic treatment and then filtered through mixed fibre film (aperture:0.22μm). The obtained membranes were dried overnight at room temperature before being reduced by immersion in diluted 40 wt. % HI solution at 85 °C for 10 h. The RGO and RGO/CNF membranes were treated by washing them with ethanol and deionized water to remove residual HI solution. The as-prepared RGO and RGO/CNFs membranes were dried overnight in a vacuum oven at 60 °C. The RGO/CNFs composite membranes were named RGO/CNFs-0.25, RGO/CNFs-0.5, RGO/CNFs-0.75 and RGO/CNFs-1.

1.3. Synthesis of RGO/CNFs@PPy composite membranes

The PPy pillar microarrays were fabricated with electrochemical polymerization by a CHI 660D electrochemical workstation. As a working electrode, the binary RGO/CNFs membrane was immersed into 0.145 M pyrrole and 0.01 M p-TSA aqueous solution

for 10 min in advance. An Ag/AgCl electrode and a platinum sheet were used as reference electrodes and counter electrodes.

Then, the electrochemical deposition was performed in the potential windows at a constant current of 0.5 mA for 5, 10, 20, 30 and 40 min, respectively. After the electrodeposition, the samples were dried overnight at 60 °C in an oven. The ternary RGO/CNFs@PPy systems were named as RGO/CNFs@PPy-5, RGO/CNFs@PPy-10, RGO/CNFs@PPy-20, RGO/CNFs@PPy-30 and RGO/CNFs@PPy-40, respectively. The PPy pillar microarrays were deposited on the RGO membrane using a similar method for comparison named RGO@PPy-20.

1.4. Assembly of the three-electrode aqueous supercapacitors (ASCs)

1M H_2SO_4 aqueous electrolyte was prepared by mixing 50 g H_2SO_4 in 500 ml deionized water (1:10, in weight) and stirring until the solution became clear. The samples of equal size taken from RGO, RGO/CNFs, RGO@PPy and RGO/CNFs@PPy composite membranes were assembled into working electrodes (effective area: 1 cm^2). The counter and reference electrodes were a platinum sheet and an Ag/AgCl electrode, respectively.

1.5. Assembly of the flexible all-solid-state micro-supercapacitors (MSCs)

6 g PVA, 60 mg $K_2S_2O_8$ and 6 g H_2SO_4 were added to 60 mL deionized water (1:1:10, in weight) and stirred at 90 °C in an oil bath until the solution became clear. 11.4 ml AA was subsequently added to the above solution and stirred for 5 min to obtain gel electrolyte. Two pieces of RGO/CNFs@PPy composite membranes were uniformly coated and sandwiched by PVA/H_2SO_4/AA gel electrolyte. The terminal of two RGO/CNFs@PPy composite membranes was connected and covered simultaneously by copper tape and conductive silver adhesive.

1.6. Fabrication of the flexible tactile biosensors

Copper tapes were attached at the end of RGO/CNFs@PPy composite membranes with conductive silver adhesive for electrical connections and dried at 60 ℃ for 5 min

to obtain tactile biosensors.

2. Characterization

The surface and cross-sectional images of the samples were captured by a field emission scanning electron microscope (SEM) system (Regulus 8100, Hitachi, Japan). The CNFs suspension was diluted to 1 mg ml^{-1} and then centrifuged at 8500 rpm for 15 min. The diluted GO suspension (1 mg ml^{-1}) was centrifuged at 8000 rpm for 15 min. Then, the lateral dimension of GO nanosheets was characterized by using an atomic force microscope (AFM) system (Dimension Edge, Bruker, Germany) after dropping supernatant to the mica flakes and drying for 12 h. The morphology of CNFs was characterized using a transmission electron microscope (TFM) system (JEM 2100, JEOL, Japan). The functional groups of RGO, CNFs, PPy and RGO/CNFs@PPy composite membrane were obtained by Fourier transform infrared spectroscopy (FTIR) system (VERTEX 80V, Bruker, Germany). The Raman spectra of the samples were recorded on a confocal Raman microscope (Raman) system (DXR532, Themor, USA) with 532 nm wavelength incident laser light. The X-ray photoelectron spectroscopy (XPS) spectra were recorded on a spectrometer (AXIS UltraDLD, Kratos) with Al Ka radiation as the excitation source. The tensile strain-strength tests of the samples (effective test length: 2 cm) were performed by a universal testing machine (CMT4202, SANS, USA) at a constant speed of 2mm min^{-1}.

The X-ray diffraction (XRD) spectra were detected in an Ultima IV X-ray diffractometer System with Cu Ka radiation. The Bragg equation calculates the interlayer spacing of all samples:

$2d\sin\theta_{002}=n\lambda$

Where d (Å) is the distance between crystal planes, n is the reflection series, λ (1.54056 Å) is the wavelength of the X-ray used, and θ is the scattering angles of the peak.

2.1. Electrochemical measurements and calculations

The electrochemical tests for ASCs were examined in a three-electrode testing system by a CHI660e electrochemical workstation. The cyclic voltammetry (CV), galvanostatic charge-discharge (GCD) and electrochemical impedance spectroscopy (EIS) measurements were tested in 1 M H_2SO_4 aqueous electrolyte.

The areal capacitance (C_A, mF cm^{-2}) of electrodes of the ASCs were evaluated from the CV and GCD curves according to the following equations:

$$C_{A-individual}=\frac{\left(\int |I|dU\right)}{2\times A\times v\times \Delta U} \quad (1)$$

$$C_{A-individual}=\frac{I\times t}{\Delta U\times A} \quad (2)$$

where I (mA) is the current, t (s) is the discharge time, ΔU (V) is the actual voltage window in the charge/discharge process, v (V s^{-1}) is the scan rate, A (cm^2) is superficial area of the electrode, respectively.

The areal capacitance (C_A, mF cm^{-2}) of a single electrode of the MSCs were evaluated from the GCD curves according to the following equations:

$$C_{A-single}=\frac{\left(\int |I|dU\right)}{A\times v\times \Delta U} \quad (3)$$

$$C_{A-single}=\frac{2\times I\times t}{\Delta U\times A} \quad (4)$$

where I (mA) is the current, t (s) is the discharge time, ΔU (V) is the actual voltage window in the charge/discharge process, v (V s^{-1}) is the scan rate, A (cm^2) is the areal of a single electrode of the MSCs, respectively.

The total areal capacitance ($C_{A\text{-entire}}$, mF cm^{-2}) of the RGO/CNFs@PPy MSCs were calculated from the GCD curves according to the following equation:

$$C_{A-entire} = \frac{I \times t}{\Delta U \times A_{(total)}} \quad (5)$$

Where t (s) is the discharge time; I (mA) is the constant current both for charging and discharging; ΔU (V) is the potential window; $A_{(total)}$ (cm^2) is the superficial area of the whole MSC respectively.

The areal energy density (E_A, μWh cm^{-2}), areal power density (P_A, μW cm^{-2}), volumetric energy density (E_V, mWh cm^{-3}) and volumetric power density (P_v, mW cm^{-3}) of the whole RGO/CNFs@PPy MSCs were calculated according to the following equations:

$$E_A = \frac{\Delta U^2 \times C_{A-individual}}{3.6 \times 8} \quad (6)$$

$$P_A = \frac{3600 \times E_A}{t} \quad (7)$$

$$E_V = \frac{A_{(single)} \times E_A}{1000 \times V_{(single)}} \quad (8)$$

$$P_V = \frac{A_{(single)} \times P_A}{1000 \times V_{(single)}} \quad (9)$$

Where $C_{A\text{-individual}}$ (mF cm^{-2}) is the areal capacitance of a single electrode of the RGO/CNFs@PPy MSCs; ΔU (V) is the potential window; t (s) is the discharge time; $A_{(single)}$ (cm^2) is the superficial area of the single electrode.

The charge storage mechanism of the RGO/CNFs@PPy MSC was defined according to the following equation:

$$i = av^b \quad (10)$$

Where i (mA) is the peak current, v (mV s^{-1}) is the scan rate, and a and b are adjustable values.

The capacitive ratio was estimated according to the following equation:

$$i = k_1 v + k_2 v^{0.5} \quad (11)$$

Where k_1v and $k_2v^{0.5}$ represent the current due to the surface capacitive effect and diffusion-controlled intercalation process, respectively.

The minimal characteristic relaxation time constant (τ), imaginary and real capacitances were calculated to evaluate the capacitance response and the time constant according to the following equations:

$$\omega = 2\pi f_0 \quad (12)$$

$$C'(\omega) = \frac{-Z''(\omega)}{\omega|Z(\omega)|^2} \quad (13)$$

$$C''(\omega) = \frac{Z'(\omega)}{\omega|Z(\omega)|^2} \quad (14)$$

$$\tau = \frac{1}{f_0} \quad (15)$$

where ω is the angular frequency, f_0 is the frequency at which the imaginary capacitance reaches the maximum, Z'(ω) and Z''(ω) is the real and imaginary parts of the Z'(ω), respectively.

Computational and simulation Details

Density functional theory simulations was performed on CP2K/Quickstep package. A hybrid Gaussian based on double-ζ MOLOPT basis sets (DZVP-MOLOPT-SR-GTH) and Goedecker-Teter-Hutter (GTH) pseudopotentials was applied. The Cutoff energy and convergence condition were set as 450 Ry and $1*10^{-6}$. Firstly, creating a heterostructure model of graphene and H_2SO_4 solution (consisting of 1 H_2SO_4 and 30 H_2O) was optimized. Meanwhile, the periodic structure was applied, and thus the work constructed such a heterostructure to save computational resources. Whereafter, the ab initio molecular dynamics (AIMD) was applied on the heterostructure, during which graphene was fixed. The time step of AIMD simulations was set as 1fs under the temperature of 303K for 2000 steps. Similarly, the heterostructures of CNF-loaded graphene were used to replace graphene for AIMD simulations. These models were labelled as Graphene and Graphene-OH-CNF, respectively.

$$D = \lim_{t\to\infty}\left[\frac{1}{2dt}\left\langle\left[\vec{r}_i(t)\right]^2\right\rangle\right] \qquad (16)$$

Here, d and t represent the calculation dimension and time; $r_i(t)$ is the displacement of i-th step for S atom. Therefore, the diffusion coefficient of S atoms for Graphene, Graphene-OH and Graphene-OH-CNF were calculated as 0.43, 0.67 and 0.51 $Å^2$/ps. It means that the diffusion coefficient of H_2SO_4 molecular in Graphene-OH and Graphene-OH-CNF is higher than that in Graphene.

The finite element simulations were performed on COMSOL Multiphysics 5.6 based on the piezoelectric module under a steady state. For elucidate the effect of structure on the piezoelectric performance, three layers graphene, sandwich-structure graphene/cellulose and surface-supported graphene/cellulose/ppy, along with Al electrode on their top, were constructed. The whole model on their bottom surface is fixed and connected with ground. A 100 N/m^2 compressive stress was applied on the Al electrode along z axis to generate stress with their deformation, and piezoelectric potential.

Supplementary Figures

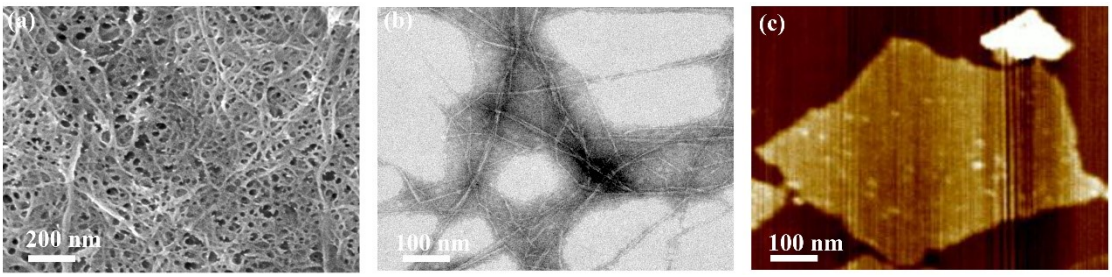

Fig. S1 (a) SEM image of CNFs. (b) TEM image of CNFs. (c) AFM image of RGO nanosheet.

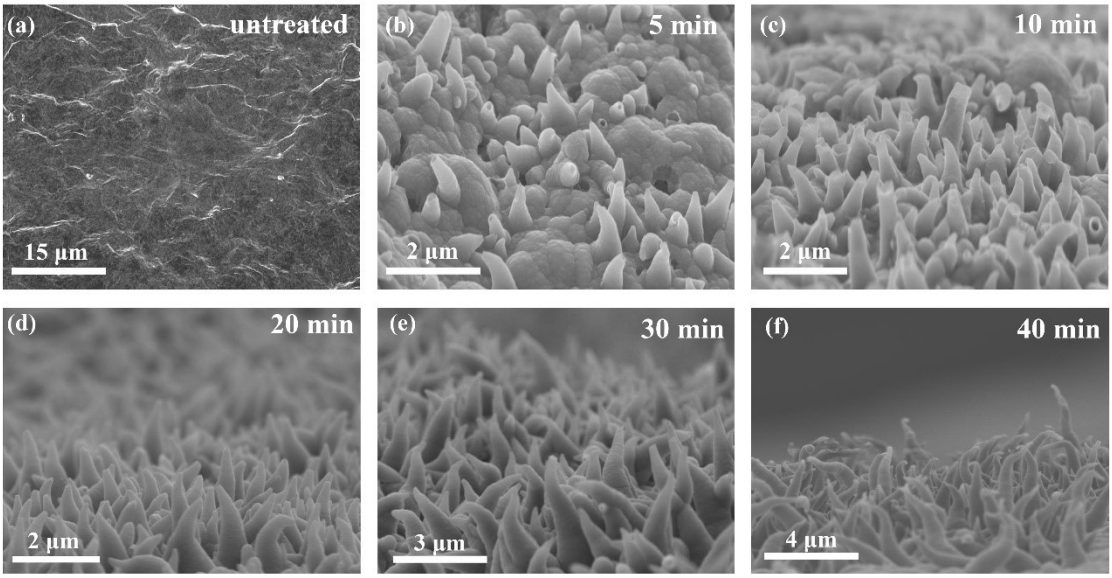

Fig. S2 (a) Surface image of RGO/CNFs binary membrane. (b-f) Surface images of PPy pillar microarrays morphology on the surface of RGO/CNFs@PPy under different electrodeposition time.

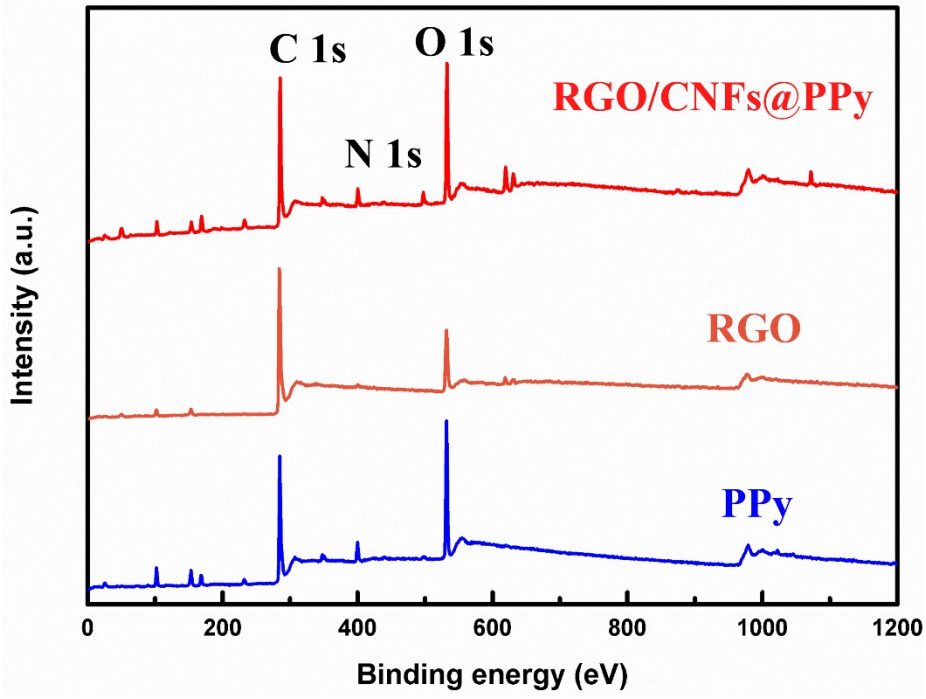

Fig. S3 XPS spectra of the RGO, PPy and RGO/CNFs@PPy.

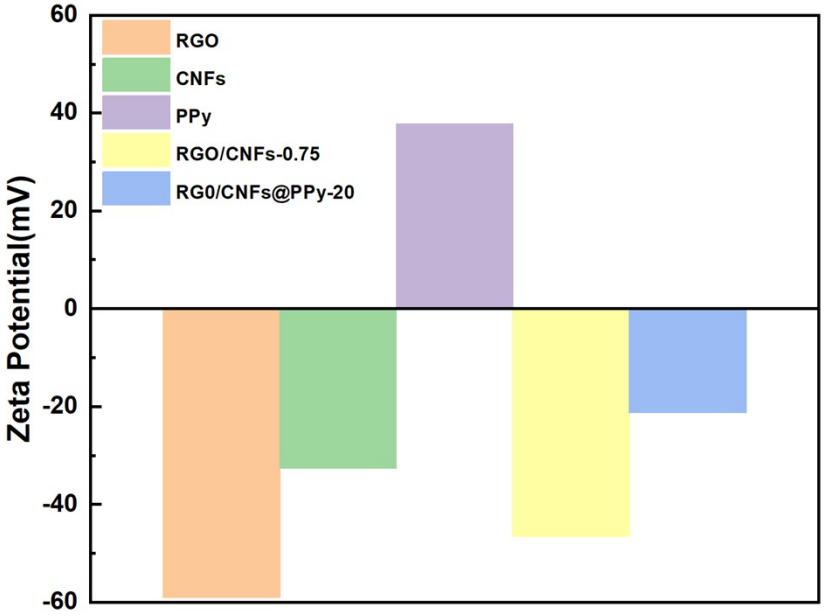

Figure S4. Zeta potential of RGO, CNFs, PPy, RGO/CNFs-0.75 and RGO/CNFs@PPy-20 aqueous dispersion.

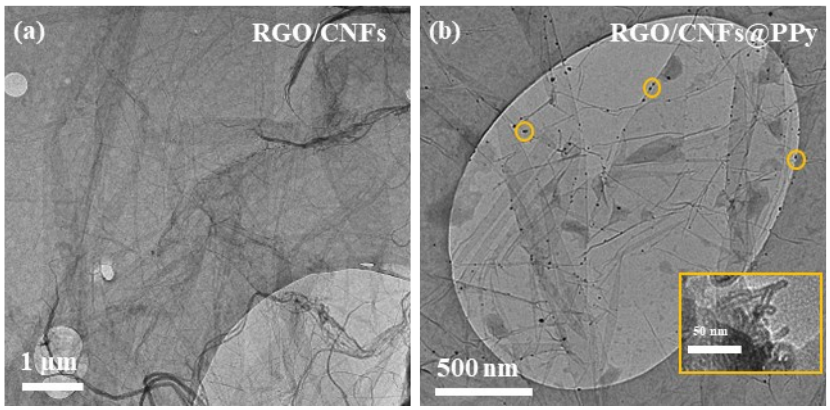

Fig. S5 HRTEM images of the (a) RGO/CNFs and (b) RGO/CNFs@PPy (PPy, inset).

Fig. S6 Water contact angle of the RGO/CNFs@PPy-20 at different times.

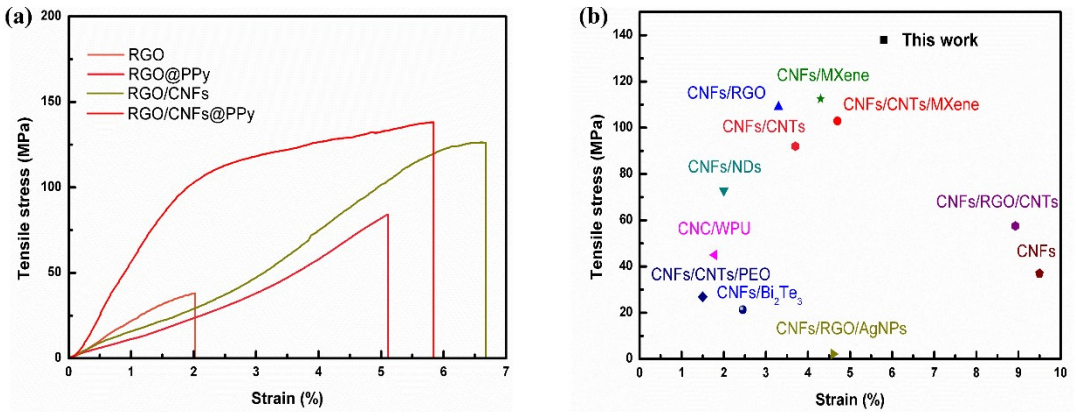

Fig.S7 (a) Tensile stress-strain curves of RGO, RGO@PPy, RGO/CNFs and RGO/CNFs@PPy. (b) Comparison of tensile stress and strain of the RGO/CNFs@PPy with CNFs and other CNFs-based composites.

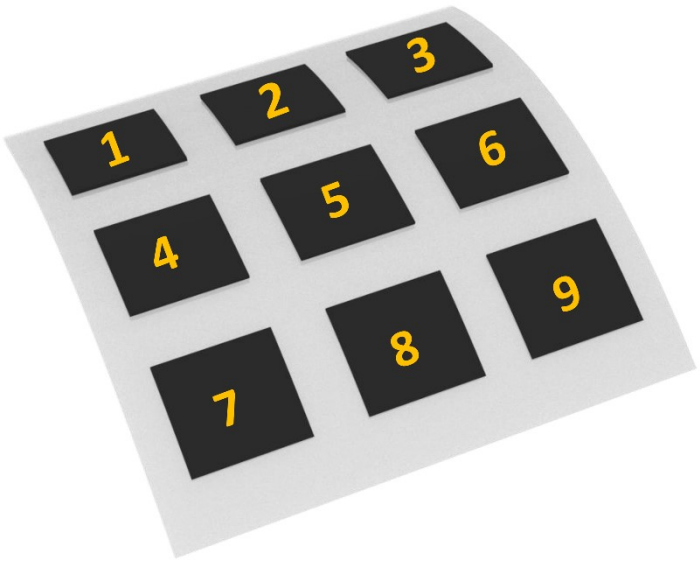

Fig. S8 The schematic diagram of the RGO/CNFs@PPy-20-array.

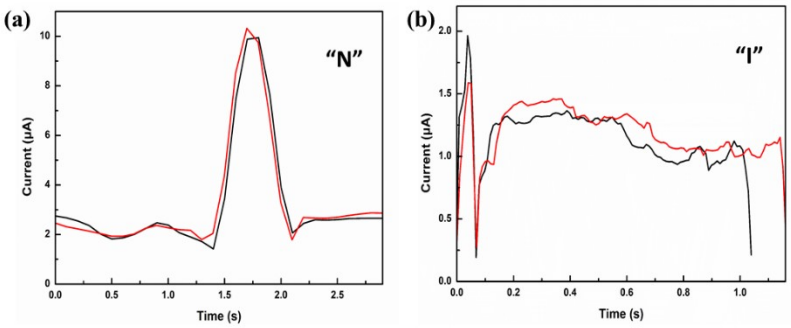

Fig. S9 The current output of RGO/CNFs@PPy-arrays under different sliding trajectory of "N" and "I", by different person.

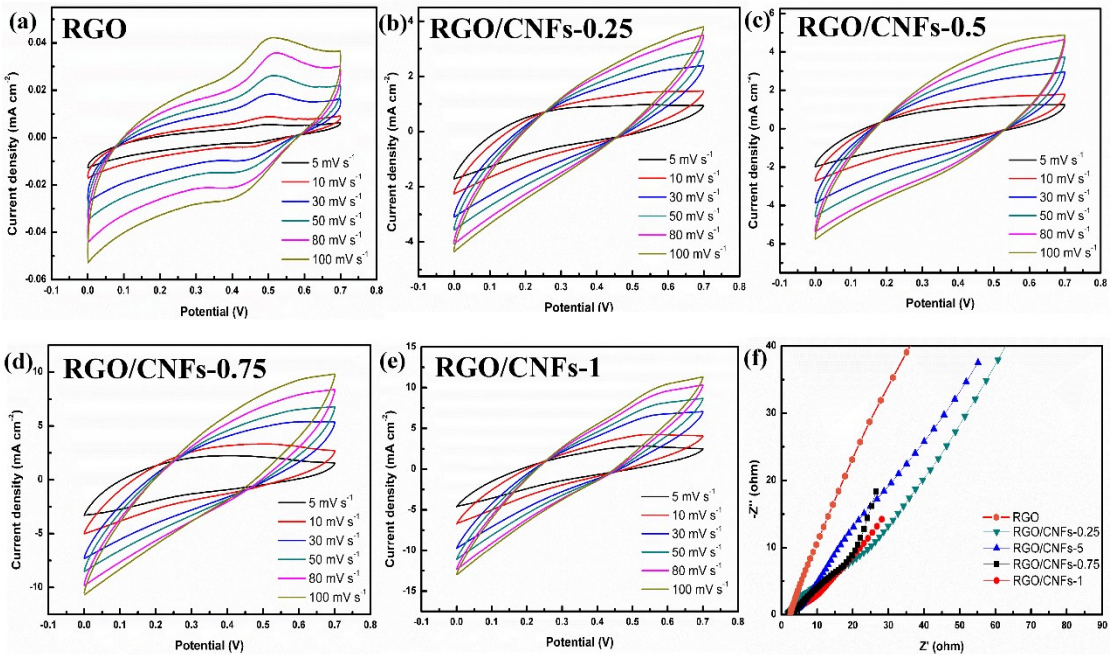

Fig. S10 Electrochemical performance of RGO, RGO/CNFs-0.25, RGO/CNFs-0.5, RGO/CNFs-0.75, and RGO/CNFs-1 in aqueous electrolyte. (a-e) CV curves. (f) Nyquist plots.

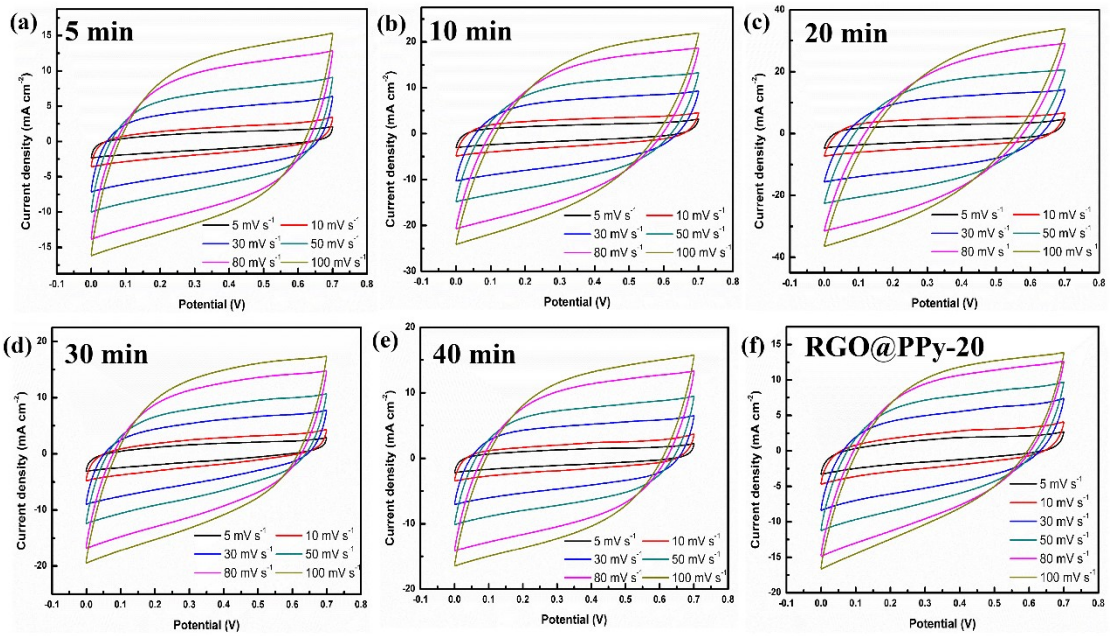

Fig.S11 CV curves of the RGO/CNFs@PPy-5, RGO/CNFs@PPy-10, RGO/CNFs@PPy-20, RGO/CNFs@PPy-30, RGO/CNFs@PPy-40 and RGO@PPy-20 in aqueous electrolyte.

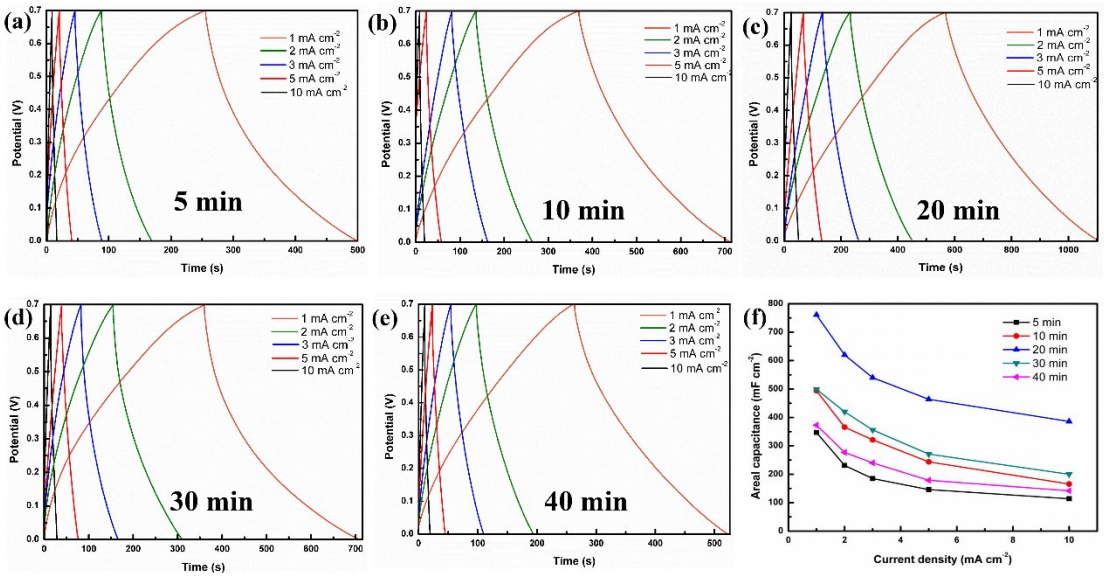

Fig.S12 Electrochemical performance of the RGO/CNFs@PPy-5, RGO/CNFs@PPy-10, RGO/CNFs@PPy-20, RGO/CNFs@PPy-30 and RGO/CNFs@PPy-40 in aqueous electrolyte. (a-e) GCD curves. (f) Rate performance.

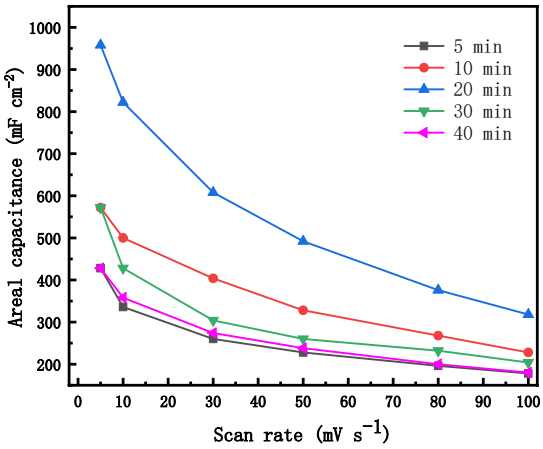

Fig. S13 Rate performance of the RGO/CNFs@PPy-5, RGO/CNFs@PPy-10, RGO/CNFs@PPy-20, RGO/CNFs@PPy-30 and RGO/CNFs@PPy-40 in aqueous electrolyte.

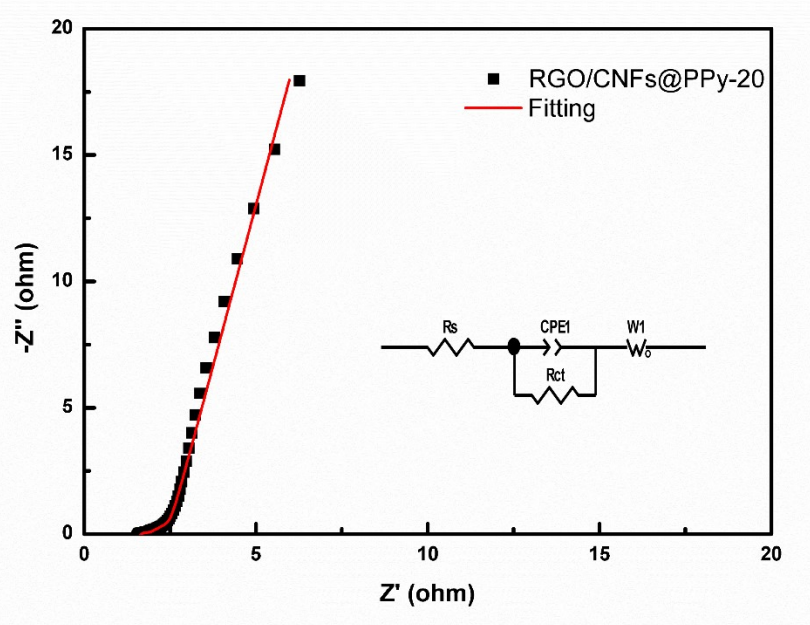

Fig. S14 Nyquist plot of the RGO/CNFs@PPy-20, the inset demonstrates the equivalent circuit.

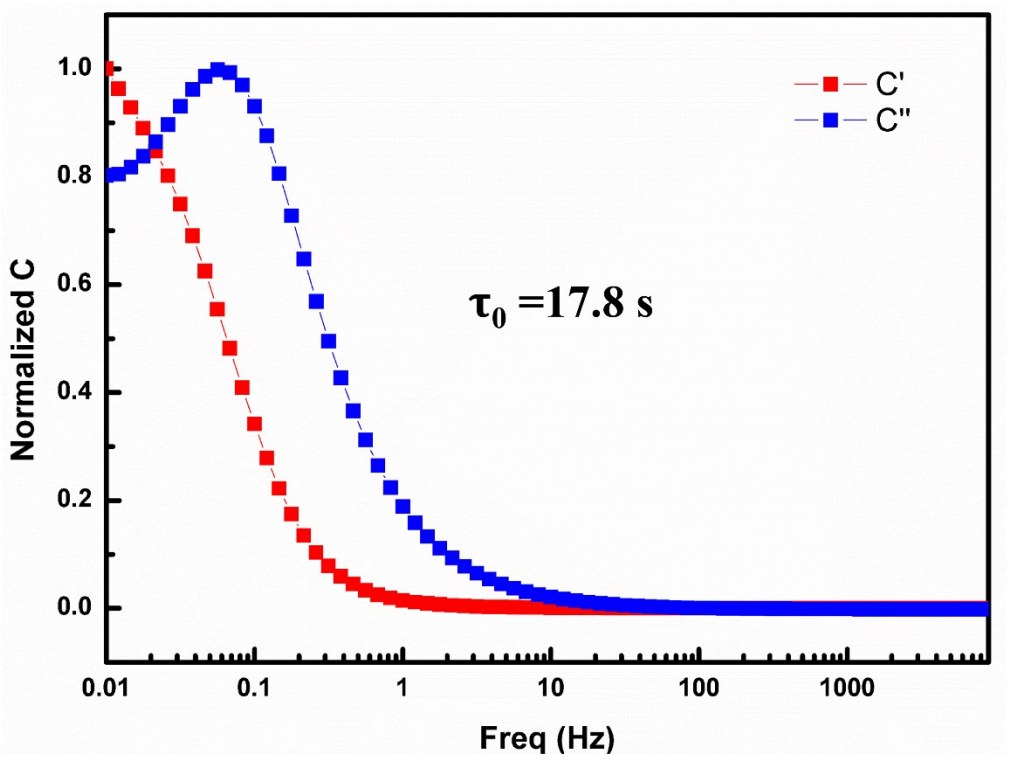

Fig. S15 Normalized real and imaginary capacitances of the RGO/CNFs@PPy-20.

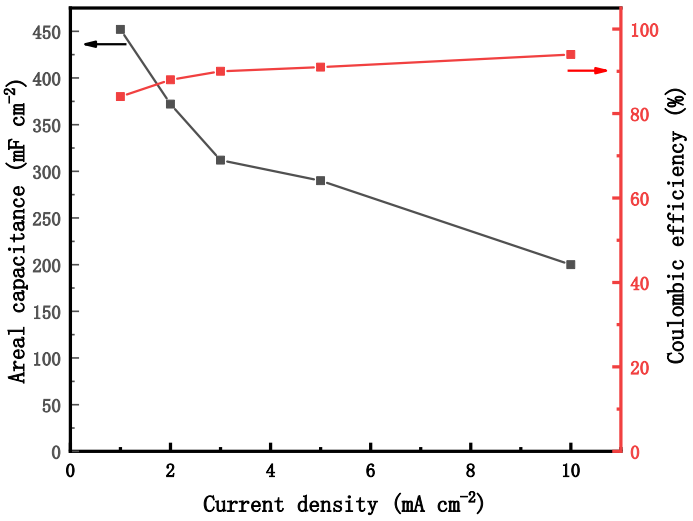

Fig. S16 Areal capacitance and coulombic efficiency of the RGO/CNFs@PPy-20 all-solid-state MSC at different current densities.

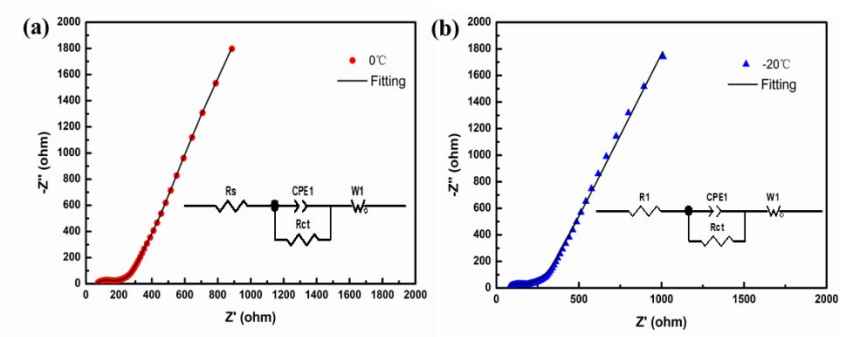

Fig. S17 Nyquist plots of the RGO/CNFs@PPy-20 MSC under different low temperature, the inset shows the equivalent circuits.

Table S1 Several mechanical properties of the RGO/CNFs@PPy compared with CNFs and other reported CNFs-based composite materials.

Materials	Strength (MPa)	Strain (%)	Reference
CNFs/CNTs/MXene	102.9	4.7	[1]
CNF/GNPs/MXene	53.52	-	[2]
CNFs/NDs	72.7	2	[3]
TOCN/RGO/PPy	72	4.79	[4]
CNFs/RGO/AgNPs	2.14	4.6	[5]
CNF/MXene-AgNWs	137	5.7	[6]
CNFs	37	9.5	[7]
CNFs/CNTs	92	3.7	[8]
CNFs/MXene	112.5	4.3	[9]
CNFs/Bi_2Te_3	21.29	2.45	[10]
CNFs/RGO/CNTs	57.7	8.9	[11]
RGO/CNFs@PPy	138	5.8	**This work**

Table S2 Areal energy and power density of the RGO/CNFs@PPy-20 MSC compared with some reported energy storage devices.

Electrode materials	Electrolyte	E ($\mu Wh\ cm^{-2}$)	P ($mW\ cm^{-2}$)	Reference
RGO PBV film	H_2SO_4/PVA	2.49	0.05	[12]
RGO/Ni yarn	H_3PO_4/PVA	1.2	0.25	[13]
RGO/PPy	LiCl/PVA	3.9	0.04	[14]
RGO/Graphite paper	H_2SO_4/PVA	1.24	0.0254	[15]
PPy@CNTs@urethane	H_3PO_4/PVA	6.13	0.133	[16]
RGO/MOFs	LiCl/PVA	1.8	7	[17]
MnO_2//PPy	Na_2SO_4/CMC	5	0.9	[18]
RGO/PPy/MnO_2	H_3PO_4/PVA	4.5	0.1	[19]
RGO/CNT/PH1000	H_3PO_4/PVA	0.54	1.22	[20]
CNT/PPy	LiCl/PVA/MPII	0.44	0.1765	[21]
MXene/BC@PPy	H_2SO_4/PVA	10	-	[22]
RGO/RuO_2	H_2SO_4/PVA	5.17	4	[23]
3D Graphene	H_2SO_4/PVA	0.38	14.4	[24]
MXene/BC	H_2SO_4/PVA	5.54	-	[25]
Graphene-cellulose	H_2SO_4/PVA	9	100	[26]
CNFs/PPy	-	6.05	2.44	[27]
RGO/CNFs@PPy-20 MSC	H_2SO_4/AA/PVA	15.7	0.25	**This work**

Table S3 Volumetric energy and power density of the RGO/CNFs@PPy-20 MSC compared with some reported energy storage devices.

Electrode materials	Electrolyte	E ($mWh\ cm^{-3}$)	P ($mW\ cm^{-3}$)	Reference
Graphene/MoS_2	H_3PO_4/PVA	7.64	9960	[28]
Graphene/PPy	H_2SO_4/PVA	2.5	397	[29]
Plasma-reduced RGO	H_2SO_4/PVA	2.5	495000	[30]
TOBC/RGO/PPy	H_2SO_4/PVA	8.8	49.2	[31]
$Ti_3C_2T_x$/RGO	H_2SO_4/PVA	16.6	37.5	[32]
MnO_2/$Ti_3C_2T_x$/RGO	LiCl/PVA	2.13	8.16	[33]
V_2O_5/ SWCNT//RGO/SWCNT	H_3PO_4/PVA	1.95	7.5	[34]
MoO_3/RGO//MnO_2/RGO	H_3PO_4/PVA	18.2	76.4	[35]
RGO/CNFs@PPy-20 MSC	H_2SO_4/AA/PVA	31.44	0.1	**This work**

Table S4 Equivalent circuit parameters of the RGO/CNFs@PPy-20 MSC obtained from the fitting results for components of the equivalent circuit fit with the EIS Spectra

Temperature (°C)	**R_s (Ω)**	**CPE-P**	**W_1-P**
25°C	56.7	0.716	0.393
0°C	63.4	0.552	0.387
-20°C	71.5	0.547	0.375

Reference

[1] W. Cao, C. Ma, S. Tan, M. Ma, P. Wan, F. Chen, Ultrathin and Flexible CNTs/MXene/Cellulose Nanofibrils Composite Paper for Electromagnetic Interference Shielding, Nano-Micro Lett. 11 (2019) 72.

[2] Q. Chu, H. Lin, M. Ma, S. Chen, Y. Shi, H. He, X. Wang, Cellulose Nanofiber/Graphene Nanoplatelet/MXene Nanocomposites for Enhanced Electromagnetic Shielding and High In-Plane Thermal Conductivity, ACS Applied Nano Materials, 5 (2022) 7217-7227.

[3] S. Yang, X. Sun, J. Shen, Y. Li, L. Xie, S. Qin, B. Xue, Q. Zheng, Interface Engineering Based on Polydopamine-Assisted Metallization in Highly Thermal Conductive Cellulose/Nanodiamonds Composite Paper, ACS Sustain. Chem. Eng. 8 (2020) 17639-17650.

[4] H. Qiang, W. He, F. Guo, J. Cao, R. Wang, Z. Guo, Layer-by-Layer Self-Assembled TEMPO-Oxidized Cellulose Nanofiber/Reduced Graphene Oxide/Polypyrrole Films for Self-Supporting Flexible Supercapacitor Electrodes, ACS Applied Nano Materials, 5 (2022) 6305-6315.

[5] Z. Zou, W. Zhou, Y. Zhang, H. Yu, C. Hu, W. Xiao, High-performance flexible all-solid-state supercapacitor constructed by free-standing cellulose/reduced graphene oxide/silver nanoparticles composite film, Chem. Eng. J. 357 (2019) 45-55.

[6] F. Zhang, P. Ren, Z. Guo, J. Wang, Z. Chen, Z. Zong, J. Hu, Y. Jin, F. Ren, Asymmetric multilayered MXene-AgNWs/cellulose nanofiber composite films with antibacterial properties for high-efficiency electromagnetic interference shielding, Journal of Materials Science & Technology, 129 (2022) 181-189.

[7] G. Hou, Y. Liu, D. Zhang, G. Li, H. Xie, Z. Fang, Approaching Theoretical Haze of Highly Transparent All-Cellulose Composite Films, ACS Appl. Mater. Interfaces 12 (2020) 31998-32005.

[8] X. Wang, P. Wu, Fluorinated Carbon Nanotube/Nanofibrillated Cellulose Composite Film with Enhanced Toughness, Superior Thermal Conductivity, and Electrical Insulation, ACS Appl. Mater. Interfaces 10 (2018) 34311-34321

[9] B. Zhou, Z. Zhang, Y. Li, G. Han, Y. Feng, B. Wang, D. Zhang, J. Ma, C. Liu, Flexible, Robust, and Multifunctional Electromagnetic Interference Shielding Film with Alternating Cellulose Nanofiber and MXene Layers, ACS Appl. Mater. Interfaces 12 (2020) 4895-4905.

[10] X. Zhao, C. Zhao, Y. Jiang, X. Ji, F. Kong, T. Lin, H. Shao, W. Han, Flexible cellulose nanofiber/Bi2Te3 composite film for wearable thermoelectric devices, J. Power Sources 479 (2020) 229044.

[11] Y. Bai, R. Liu, E. Li, X. Li, Y. Liu, G. Yuan, Graphene/Carbon Nanotube/Bacterial Cellulose assisted supporting for polypyrrole towards flexible supercapacitor applications, J. Alloy. Compd. 777 (2019) 524-530.

[12] Y. Wu, Y. Zhang, Y. Liu, P. Cui, S. Chen, Z. Zhang, J. Fu, E. Xie, Boosting the Electrochemical Performance of Graphene-Based On-Chip Micro-Supercapacitors by Regulating the Functional Groups, ACS Appl. Mater. Interfaces 12(38) (2020) 42933-42941.

[13] X. Pu, L. Li, M. Liu, C. Jiang, C. Du, Z. Zhao, W. Hu, Z.L. Wang, Wearable Self-Charging Power Textile Based on Flexible Yarn Supercapacitors and Fabric Nanogenerators, Adv. Mater. 28 (2016) 98-105.

[14] S. Ji, J. Yang, J. Cao, X. Zhao, M.A. Mohammed, P. He, R.A.W. Dryfe, I.A. Kinloch, A Universal Electrolyte Formulation for the Electrodeposition of Pristine Carbon and Polypyrrole Composites for Supercapacitors, ACS Appl. Mater. Interfaces 12 (2020) 13386-13399.

[15] A. Ramadoss, K.Y. Yoon, M.J. Kwak, S.I. Kim, S.T. Ryu, J.H. Jang, Fully flexible, lightweight, high performance all-solid-state supercapacitor based on 3-Dimensional-graphene/graphite-paper, J. Power Sources 337 (2017) 159-165.

[16] J. Sun, Y. Huang, C. Fu, Z. Wang, Y. Huang, M. Zhu, C. Zhi, H. Hu, High-performance stretchable yarn supercapacitor based on PPy@CNTs@urethane elastic fiber core spun yarn, Nano Energy 27 (2016) 230-237.

[17] H. Wu, W. Zhang, S. Kandambeth, O. Shekhah, M. Eddaoudi, H.N. Alshareef, Conductive Metal–Organic Frameworks Selectively Grown on Laser-Scribed Graphene for Electrochemical Microsupercapacitors, Adv. Energy Mater. 9 (2019) 1900482.

[18] R. Guo, J. Chen, B. Yang, L. Liu, L. Su, B. Shen, X. Yan, In-Plane Micro-Supercapacitors for an Integrated Device on One Piece of Paper, Adv. Funct. Mater. 27 (2017) 1702394.

[19] Y. Huang, H. Hu, Y. Huang, M. Zhu, W. Meng, C. Liu, Z. Pei, C. Hao, Z. Wang, C. Zhi, ACS Nano 9 (2015) 4766- 4775.

[20] H. Xiao, Z.S. Wu, F. Zhou, S. Zheng, D. Sui, Y. Chen, X. Bao, Stretchable tandem micro-supercapacitors with high voltage output and exceptional mechanical robustness, Energy Storage Mater. 13 (2018) 233-240.

[21] J. Yun, C. Song, H. Lee, H. Park, Y.R. Jeong, J.W. Kim, S.W. Jin, S.Y. Oh, L. Sun, G. Zi, J.S. Ha, Stretchable array of high-performance micro-supercapacitors charged with solar cells for wireless powering of an integrated strain sensor, Nano Energy 49 (2018) 644-654.

[22] Y. Wu, H. Hu, C. Yuan, J. Song, M. Wu, Electrons/ions dual transport channels design: Concurrently tuning interlayer conductivity and space within re-stacked few-layered MXenes film electrodes for high-areal-capacitance stretchable micro-supercapacitor-arrays, Nano Energy 74 (2020) 104812.

[23] W. Zhang, Q. Jiang, Y. Lei, H.N. Alshareef, Wettability-Driven Assembly of Electrochemical Microsupercapacitors, ACS Appl. Mater. Interfaces 11 (2019) 20905-20914.

[24] L. Zhang, D. DeArmond, N.T. Alvarez, R. Malik, N. Oslin, C. McConnell, P.K. Adusei, Y.Y. Hsieh,

V. Shanov, Flexible Micro-Supercapacitor Based on Graphene with 3D Structure, Small 13 (2017) 1603114.

[25] S. Jiao, A. Zhou, M. Wu, H. Hu, Kirigami Patterning of MXene/Bacterial Cellulose Composite Paper for All-Solid-State Stretchable Micro-Supercapacitor Arrays, Adv. Sci. 6 (2019) 1900529.

[26] M. Sevilla, G. A. Ferrero, A. B. Fuertes, Energy Storage Materials 6 (2016) 33.

[27] B. N. Wesling, G. M. V. Dias, D. Müller, R. B. Serpa, D. Hotza, C. R. Rambo, Journal of Electronic Materials 49 (2020) 1036.

[28] S.W. Kim, J. Hwang, S.J. Ha, J.E. Lee, J.C. Yoon, J.H. Jang, Ultrathin MoS2 flakes embedded in nanoporous graphene films for a multi-functional electrode, J. Mater. Chem. A 9 (2021) 928-936.

[29] J. Qin, J. Gao, X. Shi, J. Chang, Y. Dong, S. Zheng, X. Wang, L. Feng, Z.S. Wu, Hierarchical Ordered Dual-Mesoporous Polypyrrole/Graphene Nanosheets as Bi-Functional Active Materials for High-Performance Planar Integrated System of Micro-Supercapacitor and Gas Sensor, Adv. Funct. Mater. 30 (2020) 1909756.

[30] Z.S. Wu, K. Parvez, X. Feng, K. Mullen, Graphene-based in-plane micro-supercapacitors with high power and energy densities, Nat. Commun. 4 (2013) 2487.

[31] N. Sheng, S. Chen, J. Yao, F. Guan, M. Zhang, B. Wang, Z. Wu, P. Ji, H. Wang, Polypyrrole@TEMPO-oxidized bacterial cellulose/reduced graphene oxide macrofibers for flexible all-solid-state supercapacitors, Chem. Eng. J. 368 (2019) 1022-1032.

[32] X. Zhou, Y. Qin, X. He, Q. Li, J. Sun, Z. Lei, Z.H. Liu, Ti3C2Tx Nanosheets/Ti3C2Tx Quantum Dots/RGO (Reduced Graphene Oxide) Fibers for an All-Solid-State Asymmetric Supercapacitor with High Volume Energy Density and Good Flexibility, ACS Appl. Mater. Interfaces 12 (2020) 11833-11842.

[33] M. Lu, Z. Zhang, L. Kang, X. He, Q. Li, J. Sun, R. Jiang, H. Xu, F. Shi, Z. Lei, Z.-H. Liu, Intercalation and delamination behavior of Ti3C2Txand MnO2/Ti3C2Tx/RGO flexible fibers with high volumetric capacitance, J. Mater. Chem. A 7 (2019) 12582-12592.

[34] H. Li, J. He, X. Cao, L. Kang, X. He, H. Xu, F. Shi, R. Jiang, Z. Lei, Z.-H. Liu, All solid-state V2O5-based flexible hybrid fiber supercapacitors, J. Power Sources 371 (2017) 18-25.

[35] W. Ma, S. Chen, S. Yang, W. Chen, W. Weng, Y. Cheng, M. Zhu, Flexible all-solid-state asymmetric supercapacitor based on transition metal oxide nanorods/reduced graphene oxide hybrid fibers with high energy density, Carbon 113 (2017) 151-158.